Combustion and Flame 162 (2015) 4553–4565

Contents lists available at ScienceDirect

Combustion and Flame

journal homepage: www.elsevier.com/locate/combustflame

Topology and burning rates of turbulent, lean, H_2/air flames

Alberto Amato [a], Marcus Day [b], Robert K. Cheng [c], John Bell [b], Debolina Dasgupta [a], Tim Lieuwen [a,*]

[a] School of Aerospace and Mechanical Engineering, Georgia Institute of Technology, Atlanta, GA, 30332, USA
[b] Center for Computational Sciences and Engineering, Lawrence Berkeley National Laboratory, Berkeley, CA94720, USA
[c] Environmental and Energy Technologies, Lawrence Berkeley National Laboratory, Berkeley, CA94720, USA

ARTICLE INFO

Article history:
Received 8 December 2014
Revised 8 September 2015
Accepted 9 September 2015
Available online 21 October 2015

Keywords:
Premixed flames
Turbulent combustion
Leading points
Flame stretch

ABSTRACT

Improved understanding of turbulent flames characterized by negative consumption speed-based Markstein lengths is necessary to develop better models for turbulent lean combustion of high hydrogen content fuels. In this paper we investigate the topology and burning rates of turbulent, lean ($\phi = 0.31$), H_2/air flames obtained from a recently published DNS database (Aspden et al., 2011). We calculate local flame front curvatures, strain rates, thicknesses, and burning velocities and compare these values to reference quantities obtained from stretched laminar flames computed numerically in three model geometrical configurations—a counterflow twin flame, a tubular counterflow flame and an expanding cylindrical flame. We compare and contrast the DNS with these model laminar flame calculations, and show both where they closely correlate with each other, as well as where they do not. These results in the latter case are shown to result from non-flamelet behaviors, unsteady effects, and curvature-strain correlations. These insights are derived from comparisons conditioned on different topological features, such as portions of the flame front with a spherical/cylindrical shape, the leading edge of the flame, and portions of the flame front with low mean curvature. We also show that reference time scales vary appreciably over the flame, and characterizing the relative values of fluid mechanic and kinetic time scales by a single value leads to erroneous conclusions. For example, there is a two order of magnitude decrease in chemical time scales at the leading edge of the front relative to its unstretched value. For this reason, the leading edge of the front quite closely tracks quasi-steady calculations, even in the lowest Damköhler number case, $Da_F \sim 0.005$.

1. Introduction

It is well known that fuel/oxidizer composition has a strong influence on turbulent burning rates of premixed flames, at both low and high turbulence intensities [2]. These fuel/oxidizer composition sensitivities are related to Lewis number effects and species differential diffusion, and can generally be scaled with the stretch sensitivity of the mixture (e.g., the Markstein length for weakly stretched flames) [3]. However, understanding the physical mechanisms through which the thermal-diffusive properties of the mixture influence the overall turbulent burning rate, and incorporating this understanding into models, is still an open problem [2]. Lewis number effects are particularly important in lean H_2 flames, which have strongly negative Markstein lengths and local burning velocities that can significantly exceed their unstretched values. The objective of this paper is to analyze the topology and burning rate distribution in such a flame, and to compare these results to model laminar flame calculations.

It is well known from laminar flame theory that the laminar burning velocity is altered by flame strain K_S and curvature K_C, defined by [4,5]:

$$\begin{aligned} K_C &= \nabla \cdot \vec{n} \\ K_S &= -\vec{n}\vec{n} : \nabla\vec{u} + \nabla \cdot \vec{u} \end{aligned} \tag{1}$$

where $\vec{n}$ is a unit vector locally aligned with the reference iso-scalar (such as temperature) and $\vec{u}$ is the gas flow velocity vector. K_C is defined as positive when the flame is convex toward the reactants. With these expressions the total flame stretch rate is given by

$$\kappa = K_S + s_d K_C \tag{2}$$

where s_d represents the displacement speed of the isosurface at which K_S and K_C are calculated. Within the context of single-step chemistry, this sensitivity exists because the energy balance between the preheat and reaction zone is altered by misaligned convective and diffusive fluxes of heat and mass, as is the local concentration of the deficient reactant. For real fuels with multi-step chemistry, the effects are more complex, but the burning rate sensitivity to stretch exists

* Corresponding author at: School of Aerospace Engineering, 270 Ferst Drive, Montgomery Knight Building 0150, Atlanta, Georgia 30332-0150, USA.
E-mail address: tim.lieuwen@energy.gatech.edu, tim.lieuwen@aerospace.gatech.edu (T. Lieuwen).

http://dx.doi.org/10.1016/j.combustflame.2015.09.010
0010-2180/

because local species and radical concentrations, as well as temperature profiles, are altered by strain and curvature. Single step, high activation energy analyses show that the burning velocity is a unique function of flame stretch, κ, for steady state, weakly stretched flames [6]. However, for strongly stretched, or unsteady flames, the burning velocity exhibits a different sensitivity to K_S as it does to K_C [7,8].

DNS of turbulent premixed flames in the thin reaction zone regime confirm that correlations between local flame speed and flame strain/curvature exist that are consistent with laminar flame theory, but data are rather scattered (see Section 5.2 in Ref. [2]). A few studies have also attempted to compare local flame speeds calculated in DNS of turbulent flames with laminar flame calculations. Baum et al. [9] compared local heat release rates calculated in their H_2/air flame database to calculations obtained from laminar planar counterflow twin flames at the same strain rate K_S (defined in Eq. (1)). They reported that the laminar flame calculations did a poor job in predicting species profiles across the flame, as well as consumption speeds. In contrast, Hawkes and Chen [10,11] reported that the average displacement speed, s_d, of CH_4/air and CH_4/H_2/air flame elements with the same strain rate, K_S, is well predicted by computations of laminar planar counterflow flames formed by stagnating reactants against hot products. Finally, Sankaran et al. [12] showed that the average structure of the reaction zone is represented well by laminar planar counterflow twin flame computations in their DNS of a CH_4/air slot burner.

In comparing laminar and DNS results, flame strain rather than curvature is more often utilized to parameterize burning rate variations. The curvature PDFs of turbulent premixed flames are roughly symmetrical with respect to zero, while strain rate PDFs have nonzero positive mean [13]. Based on this observation, it has sometimes been assumed that zones of enhanced and diminished burning rate due to flame curvature cancel out in the mean, leaving only the influence of strain rates to explain Lewis number and preferential diffusion effects on the global consumption rate of turbulent flames [11,14]. Neglecting curvature effects may have some justification for weakly wrinkled flames (such as in the wrinkled/corrugated flamelets regime) with $Le \sim 1$ and negligible preferential diffusion of species, but this approximation is not appropriate in general [2]. First, nonlinearity and unsteadiness in the flame response may prevent the effect of positively and negatively curved flames from canceling out, even in the mean. Second, inside the flame front K_S and K_C are not independent. DNS studies [15–20] as well as experiments [21] show that K_S and K_C are negatively correlated near the reaction zone, especially at low and moderate Damköhler numbers, and their correlation coefficient tends to become more negative with decreasing Lewis number. Third, PDFs of flame curvature and strain have generally been obtained for the whole turbulent flame brush, but the controlling dynamics of the leading and trailing edges of the instantaneous front have quite different dynamics, particularly in strongly stretch-sensitive flames [22,23]. For example, the leading edge of the turbulent flame brush is by geometric necessity more positively curved than at the trailing edge, and so Lewis number and preferential diffusion effects have completely opposite influences on the local burning rate. Similarly, the chemical time scales and, hence, the ability of the flame to respond to the local time-varying stretch varies dramatically between the leading and trailing edge of the flame brush.

A fundamental goal in the study of turbulent combustion is to characterize the mechanisms through which the average reactant consumption rates increase with increasing turbulence intensity. The most common approaches in the literature utilize "global" arguments relating to flame area, due to Damköhler [24]—i.e., in constant burning velocity flames, the turbulent burning velocity increase is directly proportional to the increase in flame surface area. Fractal models, flame surface density models, *G*-equation and flamelets models are all examples of this approach [25]. For stretch-sensitive flames, some authors have attempted to generalize these ideas by additionally accounting for variations in local burning rate [2]. However, as discussed above, nonlinear effects, time scale effects, and the stretch-curvature correlation significantly complicate such efforts.

An alternative approach to understand how turbulence modifies global burning rates is based upon so-called "leading points", which are intrinsically *local* properties of the turbulent flame. This concept was originally proposed by Zeldovich [26], who described the "leading/pilot" points as the leading edge of the turbulent flame brush. In a turbulent premixed flame, the largest velocity fluctuations in the direction of propagation create convex bulges with respect to the reactants, which generate flame surface area behind them and determine the average combustion velocity. Thus, leading points are positively curved points that exist in regions where turbulent eddies induce low approach-flow velocities. The concept of leading points has been invoked by several investigators to correlate experimental turbulent flame speed data or to develop closure models for RANS/LES turbulent combustion equations [27–31].

Several studies have further argued that the flame front at the leading edge of a turbulent flame brush consists of "critically" stretched laminar flames, whose properties can be approximated using various model laminar flame geometries, including stationary curved flame balls [27,28], expanding spherical flames [32,33] or planar, counterflow twin flames near extinction [34–37]. Specifically, for negative Markstein number flames, it has been suggested that local stretch rates at the leading points approach the maximum possible laminar burning velocity, $s_{L,\max}$, which is reached at flame stretch value just below the extinction stretch rate. For example, Venkateswaran et al. [35] proved that for isothermal fronts, the local burning velocity of the leading edge of thermodiffusively unstable mixtures asymptotes to $s_{L,\max}$. The burning rate of leading points has also been modeled using empirical formulae based on an "effective" Lewis number of the mixture [30,38,39]. The present study continues earlier work specifically focused on characterizing certain aspects of the leading edge of lean H_2/air flames [40].

The objective of this paper is to characterize the structure of a strongly stretch-sensitive (negative consumption speed-based Markstein number) flame brush, with a focus on comparison of local statistics with those averaged over the entire brush. In particular, this paper analyzes:

(1) Local flame front characteristics (burning velocity, flame thickness, curvature, strain) of turbulent premixed flames; these are presented both globally, as well as conditioned on different topological features of the front
(2) How these flame front characteristics compare to those of model laminar flame calculations, and to "critically" stretched laminar flames
(3) How this comparison changes for those portions of the flame front located near the leading edge of the turbulent flame brush.

To achieve these objectives, this paper analyzes a set of direct numerical simulations (DNS) of highly stretch-sensitive flames, described by Aspden et al. [1]. These simulations consider a lean H_2/air flames ($\phi = 0.31$) at moderate and high turbulent intensities, where non-unity Lewis number and preferential diffusion have significant influences on the overall flame structure and propagation characteristics. As a consequence, these simulations represent a good data set for analysis of turbulent flame structure of highly stretch-sensitive mixtures. The DNS results are compared and interpreted within the context of a set of one-dimensional reference solutions of stretched premixed flames in several configurations, as shown in Fig. 1. The set consists of planar counterflow twin flame (PCF), a tubular counterflow flame [41] (TCF), and an expanding cylindrical flame (ECF) ignited from a pocket of burnt gases. The PCF and TCF configurations are steady-state calculations while the ECF evolves in time. It will be shown that these different geometries can effectively bracket the

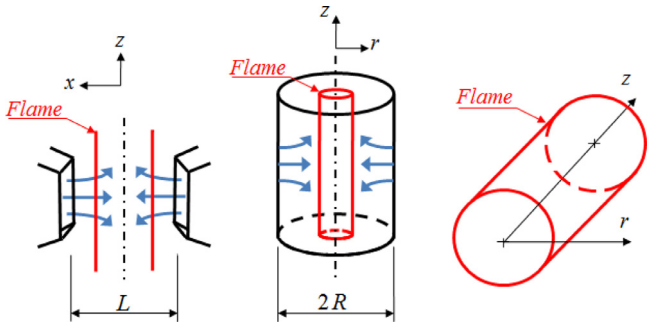

Fig. 1. Premixed flame geometrical configurations utilized in this study as model problems to investigate strongly stretched flames: planar counterflow twin flame (PCF, left), tubular counterflow flame (TCF, center), expanding cylindrical flame (ECF, right).

quasi-steady nonlinear burning velocity sensitivity to strain and curvature computed by the DNS.

The remainder of the paper is organized as follows. Section 2 presents a brief overview of the conditions and numerical methods used to compute the three model flame configurations, and summarize the DNS database of turbulent flames. Section 3 details the definitions of local burning rate, flame thickness, curvature and flame strain used in this paper to characterize the structure of the turbulent flame in terms of the 1D laminar computations. Furthermore, the procedure utilized to identify the leading edge of the turbulent flame brush is described. Results from the model laminar flame computations are presented in Section 4. Analysis of the DNS database is then presented in Section 5 for the entire flame front and conditioned at the leading edge. Section 6 concludes the study with a critical appraisal of the results obtained.

2. Numerical procedures

The DNS and model laminar flame calculations presented here utilize the transport coefficients, thermodynamics properties and chemical kinetics of the H_2/O_2 subsystem of the GRI 2.11 mechanism [42], and a mixture averaged formulation [43] to model molecular diffusion. Full details are presented in Ref. [44], with only key points about the approaches highlighted here. The analysis in Ref. [44] focused on an H_2/air flame at an equivalence ratio of $\phi = 0.31$ with unburned reactants at $T^u = 298$ K and uniform pressure $p = 1$ atm. For these conditions, a PREMIX [45] calculation shows that the unstretched laminar flame speed is $s_{L0} = 4.68$ cm/s while the flame thickness computed from the maximum value of the temperature gradient is $\delta_{T0} = (T^{b,0} - T^u)/(dT/dx)_{max} = 1.9$ mm. The adiabatic flame temperature, $T^{b,0} = 1212$ K. These numbers are used as normalization references values at various points in the paper.

For the model laminar flame calculations, the half-jet distance $L/2$ for the planar counterflow flame (PCF), and the external radius R of the entrance of fresh gases for the tubular counterflow flame (TCF), were both chosen equal to 10 cm, to ensure that the outer boundary conditions do not affect the flame structure at low strain. The expanding cylindrical flame (ECF) was initialized with temperature T, species mass fractions Y_i and gas velocity u given by

$$T(r, t=0) = \begin{cases} T^{b,0}, & 0 \le r < R_i \\ T^u, & R_i \le r < \infty \end{cases}$$

$$Y_i(r, t=0) = \begin{cases} Y_i^{b,0}, & 0 \le r < R_i \\ Y_i^u, & R_i \le r < \infty \end{cases} \qquad u(r, t=0) = 0 \tag{3}$$

These conditions correspond to a quiescent cylindrical pocket of radius R_i composed of equilibrium combustion products $Y_i^{b,0}$ at the adiabatic flame temperature $T^{b,0}$ immersed in the fresh mixture (Y^u, T^u). Calculations were performed for different initial radii, R_i, ranging from δ_{T0} to $\delta_{T0}/4$, which is close to the critical radius of ignition for these conditions, with the initial conditions smoothed over an interval of length $\delta_{T0}/10$ centered around R_i.

Table 1
Summary of DNS test cases analyzed in this paper.

Case	Turbulence Intensity, u'/s_{L0}	Turbulent straining rate, u'/l_t	Nominal Damköhler number, $Da_F = (l_t/u')/(\delta_{T0}/s_{L0})$	Leading edge conditioned Damköhler number, $Da_F = (l_t/u')/(\delta_T/s_c)$
A31	3.69	7.38 (s_{L0}/δ_{T0})	0.14	3.7
B31	17.1	34.2 (s_{L0}/δ_{T0})	0.029	1.6
C31	32.9	65.8 (s_{L0}/δ_{T0})	0.015	1.2
D31	107	213.6 (s_{L0}/δ_{T0})	0.0047	0.52

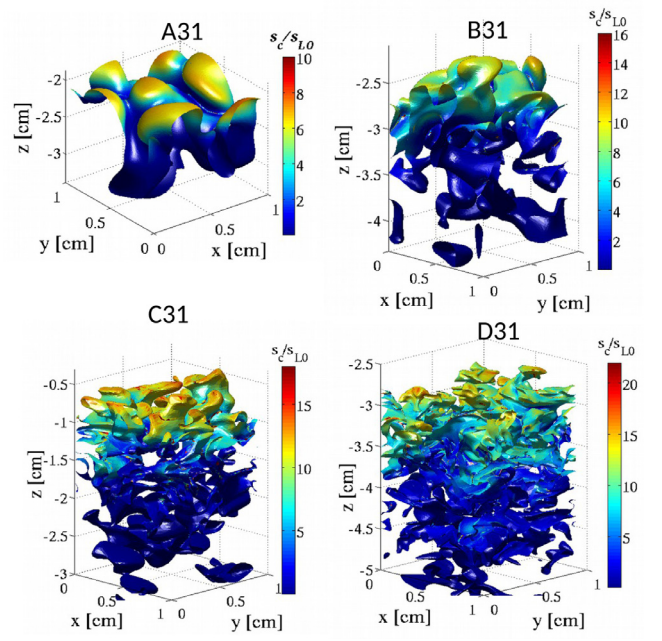

Fig. 2. Flame surface defined by the 1088 K isotherm. The surfaces are colored by the consumption speed normalized by the laminar flame speed.

The DNS database is described in detail in Ref. [1] and references therein. The simulations were performed in a computational domain consisting of a high-aspect-ratio ($5\delta_{T0}$:$5\delta_{T0}$:$40\delta_{T0}$) parallelepiped volume. The flow was initialized with fresh H_2/air mixture beneath the hot combustion products, resulting in a downward-propagating flame. Periodic lateral boundary conditions were specified, along with an insulating free-slip fixed wall at the bottom of the domain and outflow at the top. A density-weighted forcing term in the momentum equations was used to maintain the turbulent background, characterized by an integral length scale $l_t/\delta_{T0} = 0.5$. Other key parameter values are summarized in Table 1.

Sample instantaneous images of the 1088 K isotherm for these different cases are shown in Fig. 2.

3. Definitions

Burning velocities were calculated using the procedure described in Day et al. [46]. For the three-dimensional flames obtained by the DNS, this procedure starts with the tessellation of a temperature isosurface T_{ref}, and the construction of a local coordinate system by extending along integral curves, s_j, of the local temperature gradient. A prism, Ω, can then be built as shown in Fig. 3 that extends around both sides of the flame surface. The consumption speed, s_c, is then calculated by integrating the hydrogen mass consumption rate

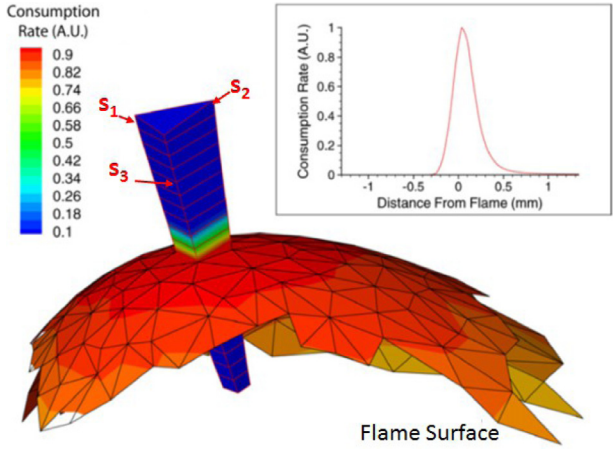

Fig. 3. Prism shaped volume, Ω, constructed using curves s_j locally normal to the temperature isotherms; the inset plot shows a typical variation of $\dot{\omega}_{H_2}$ along s_j [46].

$\dot{\omega}_{H_2}$ over the Ω volume and normalizing by the area A_{ref} intersection between Ω and the flame surface multiplied by the initial hydrogen density contained in the reactants $(\rho Y_{H_2})_{reac}$. The consumption speed is then defined as:

$$s_c = \frac{\int_\Omega \dot{\omega}_{H_2} d\Omega}{(\rho Y_{H_2})_{reac} A_{ref}} \tag{4}$$

The following analogues of Eq. (4) are used for the geometries of Fig. 1:

$$\text{PCF}: \quad s_c = \int_0^{L/2} \dot{\omega}_{H_2} dx / (\rho Y_{H_2})_{reac} \tag{5}$$

$$\text{TCF}: s_c = \int_0^{R} \dot{\omega}_{H_2} r dr / [(\rho Y_{H_2})_{reac} R_{ref}] \tag{6}$$

$$\text{ECF}: \quad s_c = \int_0^{\infty} \dot{\omega}_{H_2} r dr / [(\rho Y_{H_2})_{reac} R_{ref}] \tag{7}$$

where, for the two curved flames geometries, R_{ref} corresponds to the radial position at which the temperature is equal to T_{ref}, and $K_C = 1/R_{ref}$. The reference flame isosurface in the above definitions was chosen as the $T_{ref} = 1088\ K$ isotherm, which corresponds to the position at which the consumption rate of hydrogen $\dot{\omega}_{H_2}$ peaks in a laminar, one dimensional, unstretched flame, as calculated by PREMIX [47]. Sensitivity studies, detailed in Ref. [44], were performed by repeating these procedures using T_{ref} surfaces of 990 K and 1190 K for the model calculations and DNS showed little change in the conclusions presented later.

A flame thickness based on maximum temperature gradient, δ_T, was defined for each of the triangular elements dividing the flame surface as

$$\delta_T = \frac{1}{3} \sum_{j=1}^{3} \frac{T^{b,0} - T^u}{(dT_j/ds_j)_{max}} \tag{8}$$

where the summation is taken over the three curves emanating from the vertices of the triangular flame surface element. The length δ_T is intended to provide an estimate of the local thickness of preheat-zone. Also, note that the difference $T^{b,0} - T^u$ used to normalize the temperature gradient is purely a reference value, since the local temperature values in lean hydrogen flames differ from the adiabatic flame temperature, due to Lewis number effects and preferential diffusion of species. The analogous flame thickness definition for the 1D geometries is obtained by substituting s_j in Eq. (8) with either r for the TCF and ECF, or x for the PCF, and discarding the averaging over different s_j.

Statistical data for the DNS were gathered at twenty time instants for each case over a temporal interval approximately equal to one flame time, $\tau_{F0} = \delta_{T0}/s_{L0}$, in which the turbulent flame can be considered statistically stationary (see Fig. 7a in Ref. [1]). To identify the leading edge of the turbulent flame brush, the H_2 consumption rate field was averaged spatially at each time instant in the direction perpendicular to the mean direction of flame propagation, obtaining a one-dimensional average consumption rate profile. Based on this profile, the leading edge of the flame brush was then defined as the portion dividing the unburned reactants and the position at which the cumulative average H_2 consumption rate reaches 1/20 of the total; i.e. by defining a progress variable, $\tilde{c}$, based upon H_2 consumption, this corresponds to $0 \le \tilde{c} \le 0.05$. This particular value of $\tilde{c} = 0.05$ was chosen for practical reasons as a compromise between collecting values sufficiently close to the edge of the flame brush and having enough realizations across different snapshots in time to build meaningful statistics [44]. Sensitivity studies, detailed in Ref. [44], were performed by repeating these procedures using $\tilde{c}$surfaces of 0.025 and 0.01, without significant changes to the conclusions presented later.

4. Model laminar flame calculations

As described above, laminar premixed flames with one-step chemistry under steady state, weak stretch can be uniquely parameterized by the stretch rate, κ. Highly stretched, steady premixed flames depend nonlinearly on the spatial profiles of both strain and curvature through the flamelet, however, and cannot be described simply as a function of a reference stretch value. As such, sensitivities of the flame to large stretch values are intrinsically configuration-specific [33,48]. This section presents results from the model geometries that illustrate key features of how these laminar flames respond to stretch. The stretch rate, κ, and strain rate, K_S, are evaluated at the T_{ref} isotherm using the follow expressions:

$$\text{PCF}: \kappa = \frac{\partial u_z}{\partial z} \quad \text{TCF}: \kappa = \frac{\partial u_z}{\partial z} \quad \text{ECF}: \kappa = \frac{1}{R_{ref}} \frac{dR_{ref}}{dt} \tag{9}$$

$$\text{PCF}: K_S = \frac{\partial u_z}{\partial z} = \kappa \quad \text{TCF}: K_S = \frac{\partial u_z}{\partial z} + \frac{u_r}{R_{ref}} \quad (u_r < 0)$$

$$\text{ECF}: K_S = \frac{u_r}{R_{ref}} \quad (u_r > 0) \tag{10}$$

where u_z represents the flow velocity in the z direction (see Fig. 1) and R_{ref} is defined as in Eqs. (6) and (7).

Figure 4 reproduces plots from Ref. [44] that show the dependence of the consumption speed s_c upon flame stretch, κ, for the geometries shown in Fig. 1. With the exception of the ECF, these results all show effects of steady state stretch. Results for the ECF are plotted starting from the instant at which maximum H_2 consumption rate is reached,

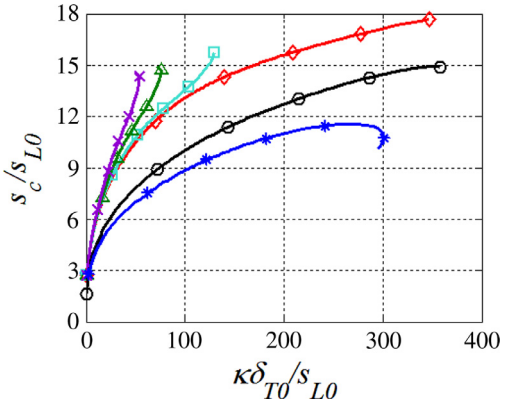

Fig. 4. Consumption speed s_c dependence on stretch rate κ for PCF "$*$", TCF "$\circ$", ECF with different initial ignition radius ($R_i/\delta_{T0} = 0.25$ "$\diamond$", $R_i/\delta_{T0} = 0.5$ "$\square$", $R_i/\delta_{T0} = 0.75$ "Δ", $R_i/\delta_{T0} = 1$ "x").

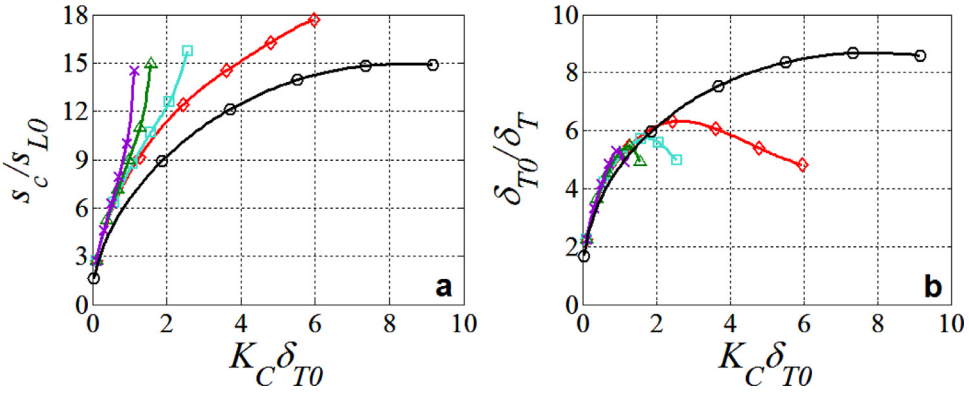

Fig. 5. Consumption rate s_c (a) and inverse of flame thickness δ_T (b) plotted against mean curvature K_C for the curved flame geometries: symbols are the same as in Fig. 4.

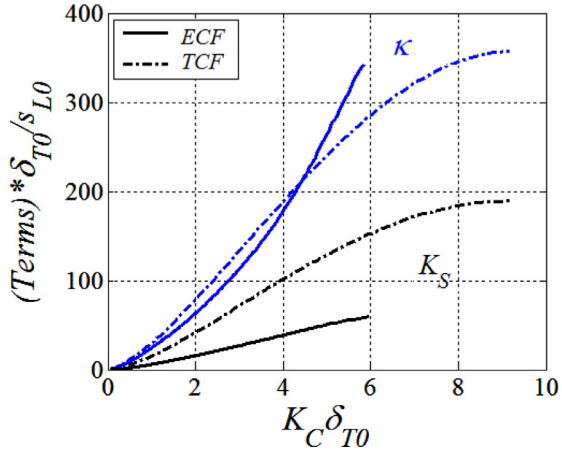

Fig. 6. Strain rate K_S and stretch rate κ dependence on curvature K_C for expanding cylindrical flame (ECF) with $R_i/\delta_{T0} = 0.25$ and tubular counterflow flame (TCF). Every quantity is calculated at the $T_{ref} = 1088$ K isosurface applying Eqs. (9) and (10)

to minimize influences of the initial phase of the ignition process. The curves suggest that for this flame, the maximum laminar consumption speeds, denoted as $s_{L,max}$, reach values 12–18 times larger than the unstretched burning velocity s_{L0}.

The curved flame results, as well as the ratio of unstretched to stretched flame thickness, δ_T, are replotted in Fig. 5a as a function of curvature, K_C [40]. The figure shows that the stretched flame thickness, δ_T, drops by up to a factor of 10 relative to its unstretched flame value. The ECF flame thicknesses display a non-monotonic behavior due to ignition transients during which the flame response is not quasi-steady [49,50]).

The Introduction noted that K_S and K_C are not independent inside the flame. In order to understand how strain and curvature are related to these model geometries, Fig. 6 plots the relationship between (a) flame stretch, κ, and (b) the strain rate K_S, upon curvature for the curved flame geometries at the $T_{ref} = 1088$ K isosurface. Figure 6 shows a close correspondence between curvature and stretch for the ECF and TCF. The strain and curvature also have a similar relationship, but the slope of the curves differs by a factor of two between the ECF and TCF. The key point from these curves is the positive correlation between curvature and strain in these model geometries. As will be discussed in the Results section, this positive strain-curvature correlation is a limitation associated with utilizing these geometries for approximating the local structure of turbulent flames, where prior studies have shown that curvature and strain are negatively correlated [15–20].

While these results illustrate the effects of time-invariant stretch on the flame, a key element of the turbulent flame is its unsteadiness. Laminar studies of flames subjected to unsteady stretch have shown that the sensitivity of the flame is not uniquely parameterized by κ, but exhibits different frequency sensitivities to strain and curvature fluctuations [8]. Generally, increasing frequencies of stretch fluctuations reduce the stretch sensitivity of the mixture, in cases where the time scales of the stretch fluctuations are shorter than characteristic chemical kinetic time scales. Figure 7 provides insight into how flame time scales vary with stretch rate, by plotting the ratio of the unstretched ($\tau_{F0} = \delta_{T0}/s_{L0}$) to stretched ($\tau_F = \delta_T/s_c$) chemical time scales versus curvature. This figure demonstrates the point, also previously emphasized by others [51], that dramatically different chemical times, and therefore Karlovitz or Damköhler numbers, will be calculated for a given set of reactants, depending upon whether nominal or stretched values are used. For the mixture considered here, this difference can be as large as two orders of magnitude. This shows that for a given unsteady straining time scale, highly stretched parts of the flame may respond in a quasi-steady manner, while other parts of the flame with slower chemistry may be highly non quasi-steady and, therefore, exhibit far less sensitivity to temporal fluctuations in stretch rate.

5. Analysis and results

This section is divided into two main parts. First, we present results of local flame front characteristics, including front topology, burning velocity, thickness, curvature, strain, and chemical times. These results are presented for the four cases of increasing turbulence intensity and compared and contrasted. Then, we compare these results to those from the model laminar flame calculations, both "globally", as well as conditioned on different parts of the flame.

5.1. Local flame front curvatures, shapes and strain rates

This section focuses on the local topological features and strain rates of the turbulent flames. Principal curvatures k_1 and k_2 ($K_C = k_1 + k_2$, $k_2 < k_1$) of the flame provide a convenient way to illustrate the relative occurrence of different topological features of the flame. These are plotted as joint distribution functions (JDF's), where the peak value of the JDF is normalized to a value of unity. Figure 8 plots JDF's, weighted by area, of the principal curvatures k_1 and k_2 of the $T_{ref} = 1088$ K isosurface for case A31 to D31. From this figure, it can be seen that the probability of larger values of curvature grows as turbulence intensity increases, and that most of the $T_{ref} = 1088$ K isosurface is convex toward the products (negatively curved $K_C < 0$), especially at high turbulent intensities. However, at positions where the $T_{ref} = 1088$ K isosurface is negatively curved, the fuel consumption rates drop considerably due to the strong stretch sensitivity of these flames. Thus, JDFs weighted by flame surface area have the undesirable effect of including large portions of non-burning surface in the statistical analysis. Thus, the strategy we adopt for most of the

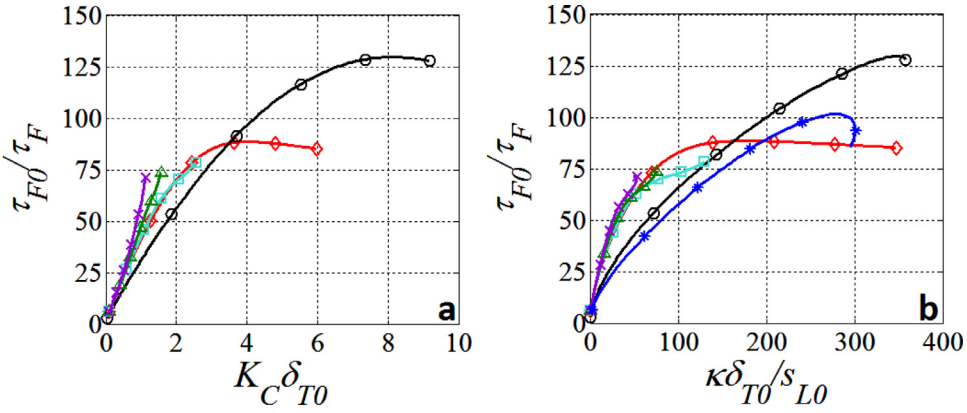

Fig. 7. Ratio of unstretched chemical time ($\tau_{F0} = \delta_{T0}/s_{L0}$) to stretched chemical time ($\tau_F = \delta_T/s_c$) plotted against (a) curvature, and (b) stretch rate (symbols are the same as in Fig. 4).

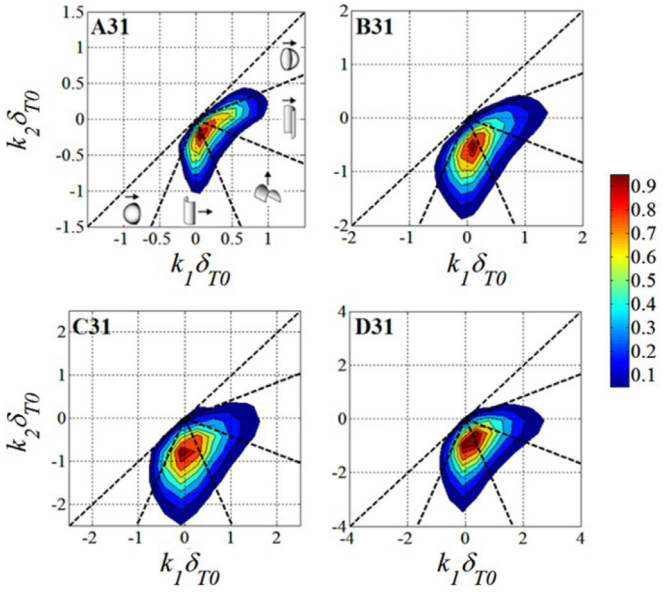

Fig. 8. Area-weighted JDFs of the principal curvatures k_1 and k_2 ($K_C = k_1 + k_2, k_2 < k_1$) of the $T_{ref} = 1088$ K isosurface for case A31, B31, C31 and D31. Small pictures in the figure of case A31, show a classification of the flame shapes in (from top, clockwise) spherical and cylindrical convex toward the fresh gases, saddle-point, cylindrical and spherical convex toward the burnt gases (arrows point toward the unburned side).

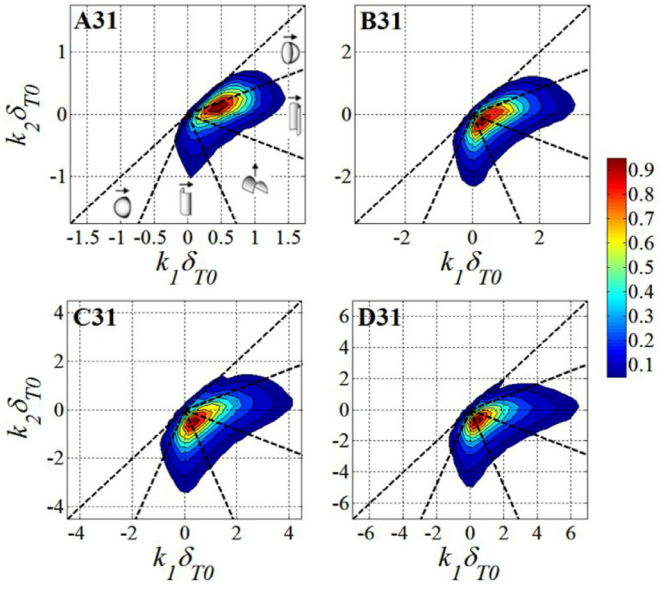

Fig. 9. Fuel consumption-weighted JDFs of principal curvatures k_1 and k_2 ($K_C = k_1 + k_2, k_2 < k_1$) of the $T_{ref} = 1088$ K isosurface for case A31, B31, C31 and D31. Legend is the same as in Fig. 8.

subsequent analysis is to weight the JDFs by the local fuel consumption, $\int_\Omega \dot{\omega}_{H_2} d\Omega$, rather than flame area, A_{ref} (see Fig. 3). With this weighting, portions of the flame front that are not burning are excluded from the analysis. Moreover, the integral of JDFs weighted by fuel consumption is more physically significant, because it is directly related to the overall reactant consumption rate.

Figure 9 shows the same data of Fig. 8, but weighted by local fuel consumption instead of flame area; clearly, much of the negatively curved portions of the $T_{ref} = 1088$ K isosurface have been excluded in these plots. The figure shows that at low turbulent intensity (i.e. Case A31), most of the fuel is consumed by flame elements with a cylindrical/spherical shape convex toward the reactants. At higher turbulent intensities, the flame becomes more tightly wrinkled and exhibits a wider variety of local geometries, including saddle-point and cylindrical shapes. Figure 9 also shows that the most highly curved elements tend to be cylindrical [52], rather than spherical.

Table 2 quantifies the fraction of fuel consumption occurring in each of the five sectors. For all cases, the majority of fuel consumption occurs in the cylindrical-toward reactants sector. With increasing turbulence intensity, however, increasing consumption also occurs in saddle-point and cylindrical toward product regions as well.

Table 2
Fraction of fuel consumption for different flame elements.

	A31	B31	C31	D31
Spherical shape convex toward reactants	0.20	0.11	0.08	0.06
Cylindrical shape convex toward reactants	0.49	0.45	0.39	0.39
Saddle point	0.16	0.19	0.21	0.22
Cylindrical shape convex toward products	0.14	0.23	0.29	0.30
Spherical shape convex toward products	0.01	0.02	0.04	0.03

These global statistics can be compared with those conditioned at the leading edge of the turbulent flame brush, $0 \le \tilde{c} \le 0.05$, as shown in Fig. 10, reproduced from Ref. [40]. This figure shows that most of the flame surface at the leading edge is cylindrically/spherically convex toward the reactants, and that the most highly curved elements tend to have a cylindrical geometry [52]. For increasing turbulent intensities, the flame becomes more tightly wrinkled and exhibits saddle-point and cylindrical-toward-products geometries, even at locations this near the leading edge. It is known that turbulent effects tend to cause material surfaces and flames to exhibit cylindrical geometries, and so this tendency toward cylindrical geometries was expected [52]. The spherical shapes that are prevalent at the lowest turbulence intensities are likely a reflection of the thermal-diffusive instability of the flame, as also discussed in Day et al.[46]

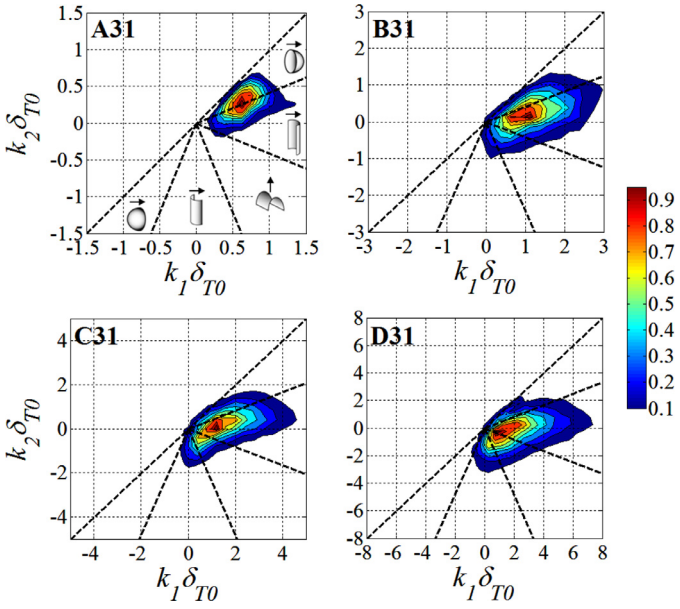

Fig. 10. Fuel consumption-weighted JDFs of the principal curvatures k_1 and k_2 ($k_2 < k_1$) at the leading edge, $0 \le \tilde{c} \le 0.05$, of the turbulent flame brush. Legend is the same as in Fig. 9.

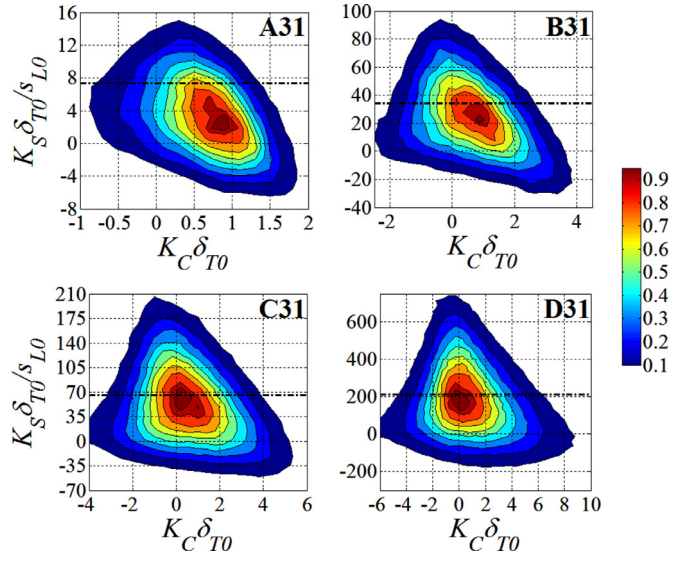

Fig. 11. JDFs of curvature K_C and strain rate K_S, weighted by fuel consumption, based on the $T_{ref} = 1088$ K isosurface for case A31, B31, C31 and D31. The height of the dot dashed lines is equal to u'/l_t.

Next, we consider the local strain rates at the $T_{ref} = 1088$ K surface and its correlation with the local curvature. Figure 11 shows the JDFs of strain rate K_S and curvature K_C, weighted by fuel consumption, for cases A31 to D31. Mean strain rate values are positive and increase with increasing turbulent intensity, consistent with prior studies [53,54]. For reference, values associated with the integral turbulent straining rate, $K_S \sim 1/\tau_t = u'/l_t$, are indicated by the horizontal lines in the plots (the values are tabulated in Table 1). The peak value of these JDFs moves to values that are quite close to u'/l_t for the higher turbulence intensity cases. Note that peak tangential strain rates are associated with near zero curvature flame elements; as explained by Pope [55], positive tangential strain acts to decrease the curvature magnitude and so this result is expected. For each case, the correlation of K_S and K_C is negative, similar to past DNS studies which considered lower turbulent intensities [15–19]. Kim and Pitsch [20] argued that this trend is a gas expansion effect and arises from defocusing of heat in front of positively curved flamelets, and vice versa for negatively curved flamelets. However, this correlation is a function of the reference surface—Kim and Pitsch showed that strain and curvature are nearly uncorrelated if a lower temperature isosurface is chosen. Similarly, strain and curvature are not correlated for isothermal turbulent propagating flames [56].

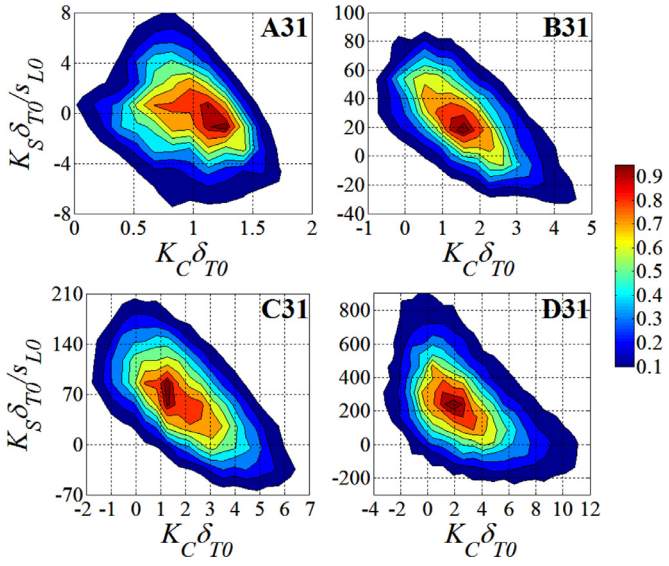

Fig. 12. Fuel consumption-weighted JDFs of curvature K_C and strain rate K_S at the $T_{ref} = 1088$ K isosurface for case A31, B31, C31 and D31 at the leading edge of the turbulent flame brush.

The JDF also shows that the largest range of K_S values occurs at locations where $K_C \sim 0$ and that the range of K_s values grows with increasing turbulence levels. Correlation coefficients (weighted by fuel consumption) between strain rate K_S and curvature K_C are displayed in the first row of Table 3. The table quantifies how the correlation between K_C and K_S decreases with increasing turbulent intensity. This is mostly due to the increasing presence of $K_C \sim 0$ portions of the flame front at higher turbulent intensities for which strain and curvature are uncorrelated, as noted above. To partially eliminate this effect, it is useful to compute the correlation coefficients between K_C and K_S considering only cylindrical and spherical (i.e., with $k_1 > k_2 > 0$) portions of the flame front, as shown in the second row of Table 3. Correlation coefficients conditioned in this way increase in magnitude, relative to the unconditioned values.

Figure 12 reproduces similar JDFs of strain rate K_S and curvature K_C as Fig. 11, but this time the data is conditioned on the leading

Table 3
Correlation coefficients (weighted by consumption speed) between strain rate K_S and curvature K_C.

	A31	B31	C31	D31
All the flame front	−0.33 (± 0.02)	−0.29(± 0.01)	−0.18(± 0.006)	−0.15(± 0.004)
Only cylindrical and spherical portions of the flame front ($k_1 > k_2 > 0$)	−0.51(± 0.01)	−0.56(± 0.01)	−0.47(± 0.005)	−0.38(± 0.004)
Only portions of the flame front at the leading edge	−0.32(± 0.05)	−0.64(± 0.02)	−0.63(± 0.01)	−0.42(± 0.008)
Only cylindrical and spherical portions of the flame front ($k_1 > k_2 > 0$) at the leading edge	−0.42(± 0.04)	−0.65(± 0.02)	−0.60(± 0.02)	−0.41(± 0.01)

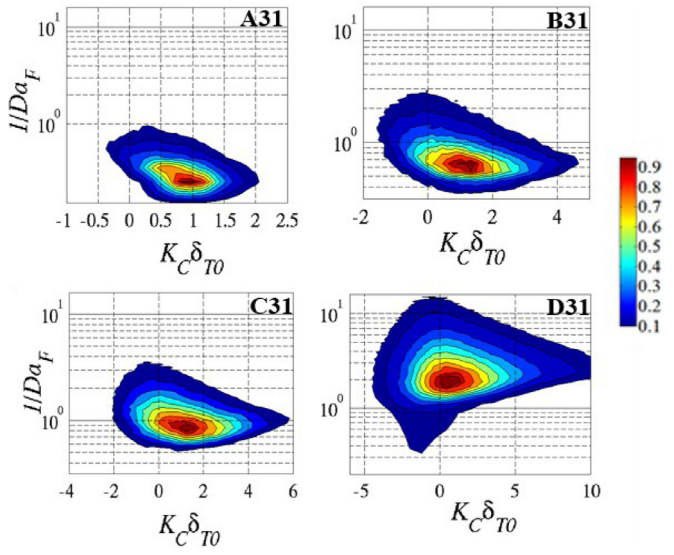

Fig. 13. JDFs weighted by fuel consumption of mean curvature and inverse of local Damköhler number $K_C - 1/Da_F$, for cases A31, B31, C31 and D31.

edge, $0 \le \tilde{c} \le 0.05$. Note that the negative correlation is stronger at the leading edge in all the cases. The values of the correlation coefficients for the portions of the flame front at the leading edge are reported in the third row of Table 3. The generally higher negative correlation at the leading edge is expected for these negative consumption speed-based Markstein length reactants, as the local gas expansion ratio is higher than its average value. As noted by a reviewer, the leading edge curvature is largely positive and a positive tangential strain rate will act to decrease the curvature magnitude [55]—this would also lead to a negative leading edge curvature-strain correlation, even in the absence of gas expansion.

Finally, it is important to note that the negative correlation of K_S and K_C differs from the correlations shown in Fig. 6 for the laminar flame calculations, for which K_S increases monotonically with K_C. This observation has important implications on the comparison between the model laminar geometries and turbulent flames, especially for highly curved flame elements, which are of interest for the study of leading point burning rate models as detailed in the next sections.

We close this section by considering time scales. Figure 13 plots JDF's of the inverse of the local Damköhler number, $1/Da_F$ (defined as $Da_F = (l_t/u')/(\delta_T/s_c)$) as a function of local mean curvature K_C. As eluded to above, this highly stretch-sensitive mixture has local time scales that range by several orders of magnitude. The range of time scales increases with turbulence intensity, but has little correlation with curvature.

5.2. Comparison of model laminar geometries with turbulent flame results

5.2.1. General comparisons

In this section we compare the local characteristics (flame speed, flame thickness, curvature and strain) of DNS results with the laminar flame computations described in Section 4. We start with Case A31, the case of lowest turbulent intensity. Figure 14 presents JDFs, weighted by fuel consumption, of mean curvature K_C and (a) burning speed s_c, (b) inverse of flame thickness, δ_T, and (c) and strain rate K_S. Results from the laminar flame computations are overlaid. In order to minimize the number of lines on the plot, results are shown only for TCF and ECF with $R_i/\delta_{T0} = 0.25$. As shown in Fig. 5, these cases largely bound the other cases. Consider first the burning speed and flame thickness. These figures show that the general structure of the JDF, particularly the peak location, is quite similar to the laminar result. However, the burning velocity-curvature sensitivity is slightly weaker than predicted by the model laminar flames calculations. The plot indicates that highly positively curved flamelets tend to burn less intensely and tend to be thicker than the model laminar flames with the same curvature, and vice versa for flat or negatively curved flamelets. The opposing signs of these sensitivities likely stem from the aforementioned difference in strain-curvature correlations between the laminar geometries and DNS data, and can clearly be seen in Fig. 5. Note how the characteristics of the strain/curvature correlation in the DNS and laminar calculations is completely different.

Much of the dispersion in the JDF data is likely due to unsteady effects in the flame response. This is supported by the fact that the ratio of unstretched chemical time (δ_{T0}/s_{L0}) to the turbulent integral time scale (l_t/δ_{T0})—i.e., the inverse of the nominal Damköhler number, $1/Da_{F0}$—exceeds unity, having values of 7.4 for this case A31 (it has values of 34 for case B31, 66 for case C31 and 214 for case D31). It is difficult to quantify this point, however, as conditioning only on regions where the local Damköhler number significantly exceeds unity reduces the number of realizations for comparison to a small set of points clustered around high consumption speed values. Some insight into non quasi-steady effects can be gained from Figs. 15 and 16 (which are discussed in more detail later), that condition on $Da_F > 0.5$ locations; however, significant non quasi-steady chemistry effects are still expected at this $Da_F > 0.5$ value. An additional factor driving the disparity between the model flames and regions of the DNS results with low and negative curvatures could be non-flamelet behaviors, such as discussed in Sec. 4.4.4 of Day et al. [46]. As a consequence, the 1D flames are not an appropriate model at these locations.

In the rest of this section, we consider the higher turbulent intensity cases (B31, C31 and D31). Figure 15 shows JDFs, weighted by fuel consumption, of thermal flame thickness, δ_T versus curvature, K_C (1st row), and δ_T versus strain rate, K_S (2nd row) for case B31, C31 and D31. Most of the fuel is consumed in flamelets that are thinner than the unstretched laminar flame δ_{T0}. In contrast to what is observed for case A31, the dependence of δ_T on both K_C or K_S is non-monotonic. As

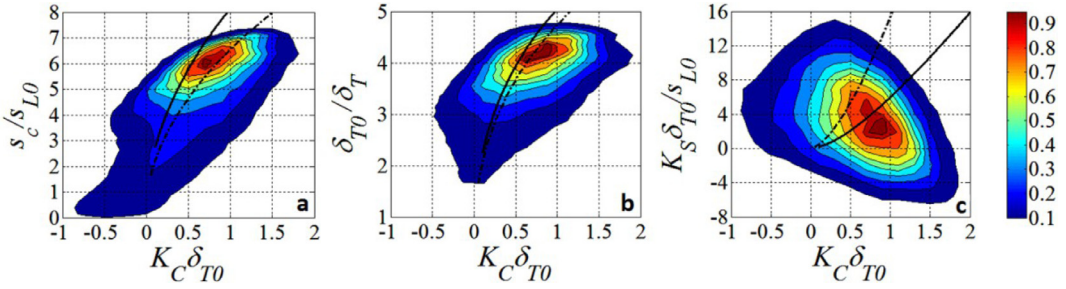

Fig. 14. JDFs for case A31, weighted by fuel consumption. Mean curvature K_C and burning speed (a)s_c, (b) inverse of flame thickness δ_T, (c) δ_{H2}, and (d) strain rate K_S. Lines superimposed on the contours refer to results obtained from one-dimensional laminar flame computations (see Fig. 5); dot-dashed lines refer to TCF computations, solid lines refer to ECF computations with $R_i/\delta_{T0} = 0.25$.

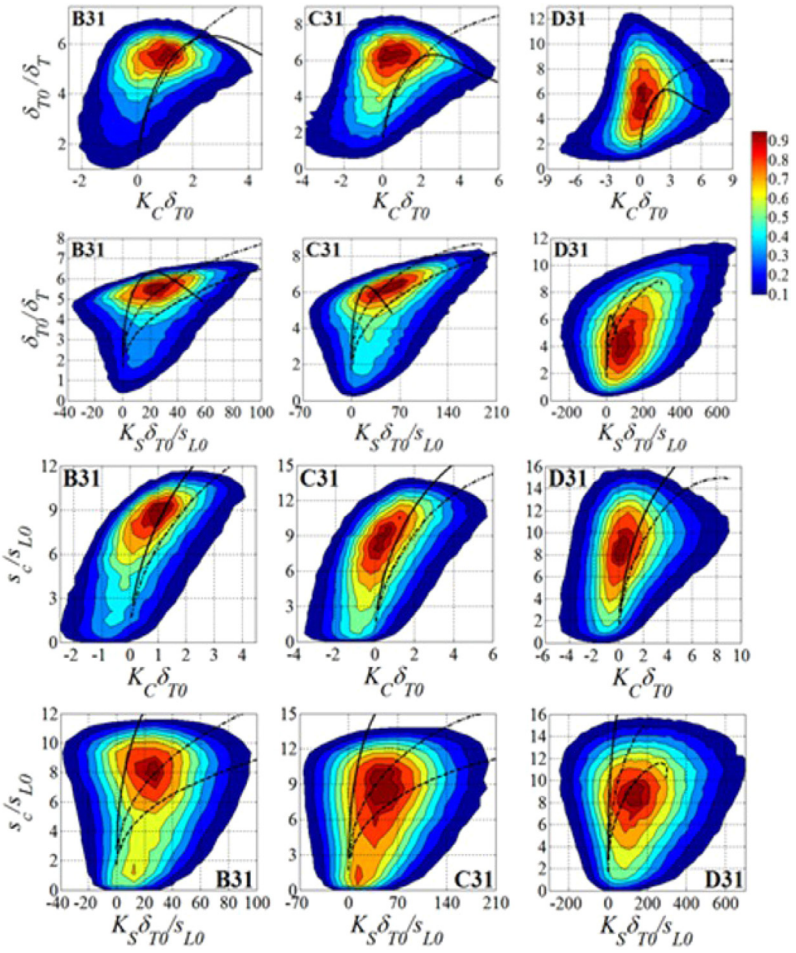

Fig. 15. Fuel consumption-weighted JDFs $K_C - \delta_T$ (1st row),$K_S - \delta_T$ (2nd row), $K_C - s_c$ (3rd row) and $K_S - s_c$ (4th row) for case B31, C31 and D31. Thick lines indicate results from laminar flame computations: dot-dashed lines refer to TCF computations, solid lines refer to ECF computations with $R_i/\delta_{T0} = 0.25$, dashed lines refer to PCF computations (shown only for the $K_S - \delta_T$ figures.).

seen in the 2nd row of Fig. 15, it is clear that δ_T is monotonically related to K_S only in regions where the flame is sufficiently thin and the strain rate is sufficiently positive. The negative correlation between strain rate and curvature is also consistent with the negative correlation between δ_{T0}/δ_T and K_C, for $K_C > 0$. These trends are consistent with those of past DNS studies with single step chemistry [18,19] and complex chemistry [57].

Figure 15 shows the JDFs, weighted by fuel consumption, for consumption speed s_c with curvature K_C (3rd row) and strain rate K_S (4th row) for case B31, C31 and D31. These figures indicate that the unconditioned consumptions speeds correlate better with local mean curvature than strain rate, in contrast to the behavior of the local thermal flame thickness δ_T. This shows that strain and curvature exert different influences on thermal gradients and the reaction zone. Similar observations were made for a stoichiometric H_2/air flame ($\phi = 1.0$, $T^u = 700$ K, $u'/s_{L0} = 1.74$, $l_t/\delta_{T0} = 2$) by Tanahashi and Fujimura [57], (see Fig. 8 in the cited paper) while the flame thickness behaved as in Fig. 15 (see Fig. 9 in the cited paper). Furthermore, Fig. 16 shows that the consumption speed is positively correlated with curvature (as expected for these negative Markstein number flames) and the data become more scattered as the turbulence intensity increases. In contrast, the dependence on strain is more difficult to interpret and no correlation is easily distinguishable.

Figure 16 shows the same results as in Fig. 15 but conditioned on locations where the local Da_F value exceeds 0.5, in order to remove regions where the local chemistry will be significantly not quasi-steady. Note how the sensitivity to curvature is not captured by the model calculations for case D31, showing the significance of tangential straining in modifying the local burning rate.

Given the complexity of the trends described in Figs. 15 and 16, it is clear that a direct comparison between laminar flame models and local statistics of the turbulent flame structure has to be performed with significantly more care than in the low turbulence intensity case A31. As shown in the next sections, this is partly due to the increased geometrical complexity of the flame front. In addition, it is also due to the stronger interaction between curvature and strain rate and the growing influence of unsteady effects for these three cases compared to case A31. For this reason, the next two sections further analyze these results by conditioning on different geometries in the instantaneous turbulent flame structures.

We next present statistical data collected at the leading edge of the turbulent flame brush, reproducing the burning velocity results from Ref. [40] and further explaining those results by reference to the curvature-strain correlation. These leading edge statistics are area weighted (area and fuel consumption weighting lead to nearly identical results, as this is a strongly-burning region). The mean, μ, and standard deviations, σ, of quantities calculated at the leading edge are calculated as:

$$\mu = \left(\sum_i A_{ref,i}\, x_i\right) \Big/ \left(\sum_i A_{ref,i}\right)$$
$$\sigma = \sqrt{\left(\sum_i A_{ref,i}\,(x_i - \mu)^2\right) \Big/ \left(\sum_i A_{ref,i}\right)} \qquad (11)$$

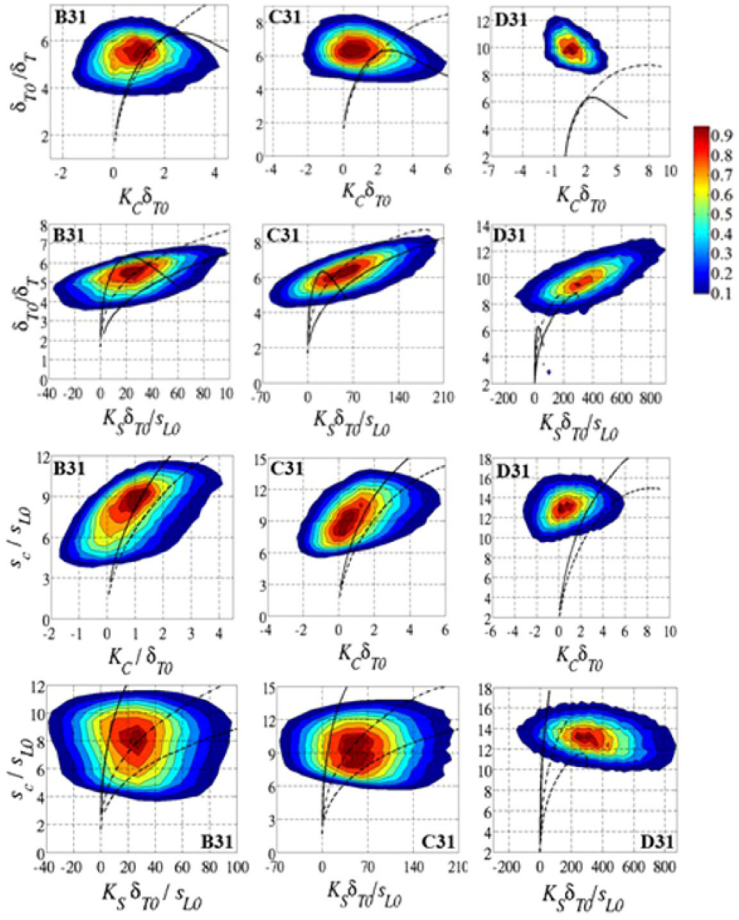

Fig. 16. Fuel consumption-weighted JDFs $K_C - \delta_T$ (1st row),$K_S - \delta_T$ (2nd row), $K_C - s_c$ (3rd row) and $K_S - s_c$ (4th row), conditioned on points where the local $Da_F > 0.5$. Thick lines indicate the results from laminar flame computations: dot-dashed lines refer to TCF computations, solid lines refer to ECF computations with $R_i/\delta_{T0} = 0.25$, dashed lines refer to PCF computations (shown only for the $K_S - s_c$ figures.).

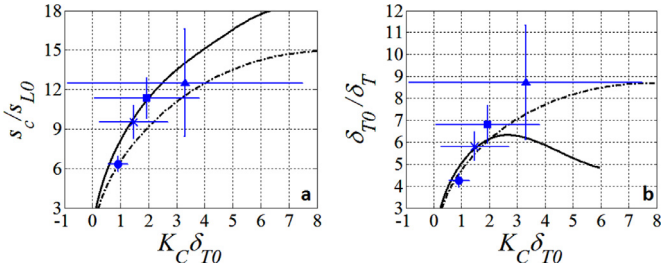

Fig. 17. Leading edge mean consumption rate s_c (a) and mean of the inverse of flame thickness δ_T (b) plotted against leading edge average mean curvature K_C. Symbols refer to different DNS cases (A31 "•", B31 "x", C31 "■" and D31 "▲"). The total length of the error bars is equal to σ on each side. Thicker solid lines refer to ECF computations with $R_i = \delta_{T0}/4$ while thicker dot-dashed lines refer to TCF computations. Reproduced from Ref. [40].

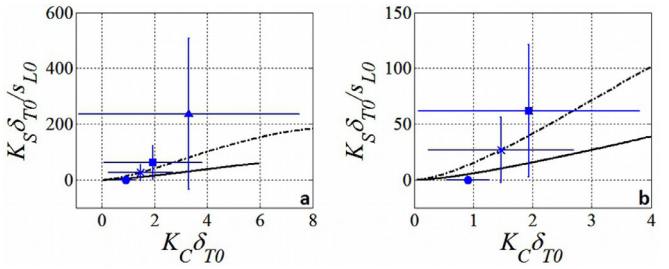

Fig. 18. Leading edge mean strain rate K_S plotted against leading edge average mean curvature K_C. Figure (b) shows a magnified view of Fig. (a) centered on case A31, B31 and C31. Legend is the same as Fig. 17.

where $A_{ref,i}$ denotes the area of the ith triangular element (see Fig. 3) and x_i represents mean curvature K_C, strain rate K_S, consumption speed s_c or flame thickness,δ_T.

Figure 17 overlays the mean and standard deviation of burning velocity and flame thickness as a function of mean leading edge curvature for the four different turbulence intensity cases. Figure 17a shows that the 1D laminar simulations computed at the average value of mean curvature reasonably follow the enhancement in consumption speed with increasing turbulence intensity. Figure 17b, however, shows that the structure of the thermal layer as measured by δ_T, is captured by the 1D simulations up to case B31, but cases C31 and D31 seem to progressively diverge from this solution. This effect is presumably due to the influence of strain, since Fig. 18 shows that, for the same values of curvature, these cases are characterized by higher strain rates than the model laminar flame computations. Figure 10 shows that, at the leading edge, flamelets with low curvature continue to exist, especially at high turbulent intensities. For these flamelets, the contribution of curvature to the total stretch rate is likely to be less important than the contribution of strain rate, accounting for some of the differences between model laminar computations and statistics obtained from the DNS. To partially eliminate these effects, Figs. 19 and 20 reproduce the results of Figs. 17 and 18, but excluding flame elements that are not cylindrically or spherically shaped; i.e., considering only those portions of the flame front for which $k_1 > k_2 > 0$. These figures show that the agreement of the flame thickness with the model laminar flame calculations is better than those in Fig. 17, except for the case D31 burning velocity.

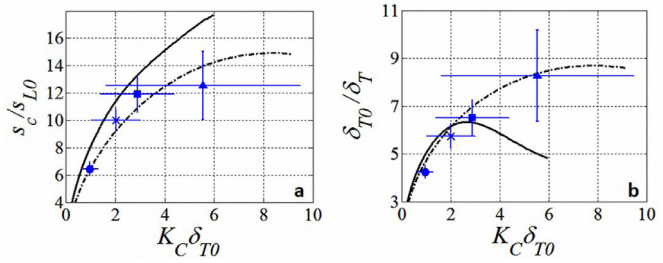

Fig. 19. Leading edge mean consumption rate s_c (a) and mean of the inverse of flame thickness δ_T (b) plotted against leading edge average mean curvature K_C. Results conditioned on positions of positive principal curvatures of the $T_{\text{ref}} = 1088$ K isosurface ($k_1 > k_2 > 0$: cylindrical and spherical elements). Legend is the same as Fig. 17.

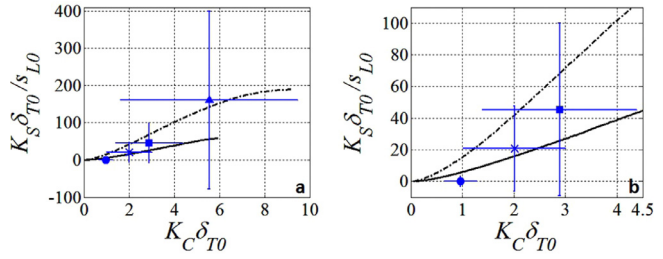

Fig. 20. Leading edge mean strain rate K_S plotted against leading edge average mean curvature K_C. Results conditioned on positions of positive principal curvatures of the $T_{\text{ref}} = 1088$ K isosurface ($k_1 > k_2 > 0$: cylindrical and spherical elements). Figure (b) shows a magnified view of Figure (a) centered on case A31, B31 and C31. Legend is the same as Fig. 17.

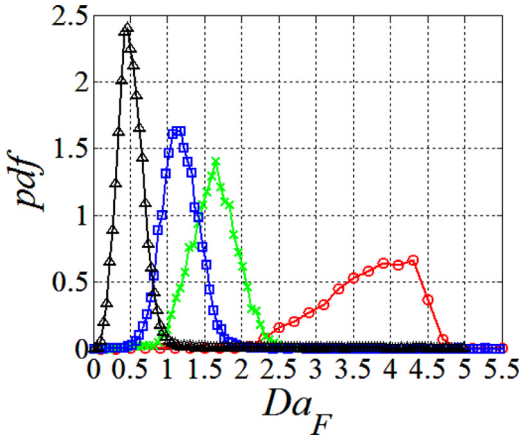

Fig. 21. Probability density functions at the leading edge (weighted by area) of Damköhler number defined as $Da_F = \tau_T/\tau_F = (l_t/u')/(\delta_T/s_c)$. Symbols refers to different DNS cases (A31 "○", B31 "x", C31 "□" and D31 "Δ"). Average values for each case are tabulated in Table 1.

This agreement was not necessarily expected, as it is known that non-steady effects decrease the effective stretch sensitivity of the flame [9,58], and so we had anticipated the DNS results for consumption speed to fall below the laminar calculations. This result might be a manifestation of the insensitivity of curvature-induced flame speed modifications to frequency, as opposed to its strong sensitivity to nonsteadiness in hydrodynamic stretch [59], that is suggested by theory. In addition, the chemical time scales at the leading edge are much lower than their unstretched value; for example, for the model laminar flame computations they differ by two orders of magnitude as shown in Fig. 7. To further illustrate, Fig. 21 plots the pdfs weighted by area of the local Damköhler number (defined as $Da_F = (l_t/u')/(\delta_T/s_c)$) for the flame front at the leading edge (where l_t and u' are global values; δ_T and s_c are calculated locally). This figure shows that local chemical time scales $\tau_F = \delta_T/s_c$ remain of the same order of magnitude as the eddy turnover time $\tau_T = l_t/u'$ with increasing turbulent intensity passing from case A31 to D31. Only case D31 has a mean value of less than unity, while cases A31–C31 all exceed unity. In contrast, the values of Da_F based upon unstretched values are all substantially less than unity, varying from about 0.005 to 0.1, as shown in Table 1. Note also that while the Damköhler number based upon unstretched values varies by a factor of about 30 between case A31 and D31, its average varies by less at the leading edge—by about a factor of 7 as shown in Table 1, which summarizes average values of the local Damköhler number.

These results enable further insight into the observations previously made by the authors in Ref. [40], which assessed the hypothesis described in the introduction that the leading edge of the flame was "critically stretched"—i.e., that the local burning velocity approached its maximum value, $s_{L,\max}$, and that the stretch rate at the leading edge approached the corresponding critically stretched value. Given the configuration-specific nature of $s_{L,\max}$emphasized previously, it is difficult to make a precise assessment, but, in terms of orders of magnitude, these comparisons show that curvatures and burning velocities can be similar to those of "critically" stretched laminar flames at high turbulent intensities. For the highest turbulent intensity case (case D31), burning rates do appear to approach the computed range of $s_{L,\max}$ values. However, burning rates are well below this value in the lower turbulence intensity cases. The fact that the leading edge burning rates and curvature values are significantly lower than critically stretched values may be, in part, be a manifestation of the negative $K_S - K_C$ correlation shown in Fig. 11 and Fig. 12. The essence of the critically stretched leading point argument put forward in Ref. [35] for isothermal fronts is that positive curvature leads to an enhanced burning velocity, which then further increases leading edge curvature, and so forth. This causes the maximum in the $s_c - K_C$ curve to serve as an attracting point. In reality, the most highly curved leading edge flamelets are also subject to compressive strain rates, which diminishes the "gain" of the $s_c - K_C$ feedback described above in the isothermal case, and prevents the flame from becoming too curved for a given level of turbulent intensity, and, thus, from reaching a critically stretched structure. For highly curved flamelets, the importance of wrinkling and stretching by turbulent eddies is apparently overcome by gas expansion effects.

5.2.2. *Results conditioned on other topological features*

We conclude this section by briefly discussing results of conditioning on flamelets with low curvature and positively curved spherical/spherical flamelets. Although not reproduced here for space, the lead author's thesis [44] presents analogous plots to those shown above for these cases.

Consider first flamelets with low curvature. As shown in Fig. 22, which plots the consumption weighted PDF of K_c for the four cases, low curvature regions occur most frequently. This was also shown

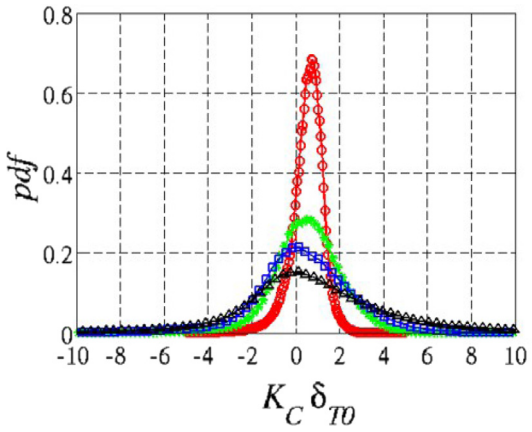

Fig. 22. Probability density functions of K_c (weighted by S_c). Symbols refers to different DNS cases (A31 "○", B31 "x", C31 "□" and D31 "Δ").

in Fig. 9, for case B31, C31 and D31, also showing that much of the fuel is consumed by flame elements with $K_C \sim 0$ (i.e. $k_1 + k_2 \sim 0$); the importance of these elements increases with increasing turbulence intensity. Moreover, Table 2 shows that roughly 22% of the fuel consumption occurs in saddle points for case D31. Although not shown for space, we briefly summarize the analysis of flame elements with low curvature by considering only portions of the flame front at which the mean curvature of the $T_{\text{ref}} = 1088$ K isosurface is less than one-tenth of the unstretched thermal flame thickness (i.e. $|K_C \delta_{T0}| < 0.1$), summarizing detailed results in Ref. [44]. These analyses show that the fuel consumption weighted JDFs of strain rate K_S with consumption speed, s_c, and flame thickness,δ_T, are well represented by PCF computations for the lower turbulence intensity cases, while for case D31 there is no agreement. In other words, the dispersion in the data characterizing these JDFs increases with turbulence intensity until the PCF computations cease to track the computations. We bring these points up to emphasize the need for further focused analysis of saddle-type topological features, both from DNS as well as for laminar flame calculations, similar to what has been done for curved or strained flames.

Consider next the analysis conditioned on positively curved spherical/cylindrical flames, detailed in [44]. These topological features were extracted by conditioning on flame elements with positive principal curvatures $k_1 > k_2 > 0$ (see Fig. 9). Similar to Fig. 14, the position of the JDFs peak probability falls on top of the model laminar flame computations and this peak probability occurs at substantially higher values of curvature and consumption speed and substantially lower values of flame thickness than for case A31. On the contrary, the overall dependence of s_c and δ_T does not agree with the model laminar flame calculations. It is not clear if this behavior is due to the fact that strongly curved flamelets are negatively strained contrary to the 1D laminar flame models described in this paper or is due to unsteadiness in the flame response.

6. Conclusions

This paper details a study of the structure of turbulent lean, H_2/air flames and a comparison with results obtained from several highly-stretched, model geometries. This type of information is useful for modeling purposes and can be compared to similar attempts to collapse flame speed data obtained by DNS of turbulent flames using different planar laminar flame models [9–12]. Many factors need to be accounted for when comparing local turbulent flame structure and model laminar flame computations, including unsteadiness in the flame response, non-flamelet behaviors, and correlations between flame front curvature and local strain rate. In order to investigate this latter phenomenon in more detail, several strategies for conditioning the DNS data have been presented.

First, expanding on previous results obtained by the authors [40], it is shown that at the leading edge of the turbulent flame brush, where strongly positive curved flamelet geometries dominate the topology of the flame front, the average structure of the flame front is represented reasonably well by quasi-steady laminar calculations even at very high turbulent intensities. For the highest turbulent intensity case, the average values of strain rate, flame thickness and fuel consumption speed are comparable to the highest values of these quantities obtained by model flame computations, particularly when only spherical and cylindrical flamelets are considered. The success of quasi-steady model laminar flame computations in capturing the structure of these flamelets, even in these very low Damköhler number flames is traced to the two order of magnitude decrease of the *local* flame characteristic time scale τ_F .This result modifies the points from Savard and Blanquart [60], who suggest that mixtures whose quasi-steady burning rates are strongly stretch sensitive, essentially revert to stretch insensitive flames at high turbulence intensities due to unsteady effects. In particular, this analysis shows the limitations of using average Damköhler number values to characterize the mixture for such flames.

Secondly, it is shown that the local structure of the case with the lowest turbulent intensity (case A31) correlate well with local flame front curvature and this correlation is similar to that existing in the curved model laminar flame geometries (tubular flame and expanding cylindrical flame). The main difference is the relation between curvature and strain rate; in the turbulent flame, curvature and strain rate are negatively correlated while the model laminar flames are positively correlated. This different relation between curvature and strain rate makes a direct comparison between the model laminar flame and the turbulent flame difficult for the cases with higher turbulent intensities (case B31, C31 and D31), for which mean strain rates have higher values. For this reason, different topological features are considered separately. In particular, the relationships between the structure of flamelet with low curvature and local strain rates is similar to results obtained from planar counterflow flames, except for the highest turbulent intensity investigated (case D31). For cylindrically and spherically shaped elements, however, only the overall trends of increasing local consumption speed and decreasing flame thickness with increasing turbulent intensity are correctly captured by the model curved geometries, while the negative correlation between curvature and strain appear to dominate the local structure of the turbulent flame.

This work highlights merits and limitations of model laminar flame computations in reproducing the structure of turbulent flames and seems to suggest that at low turbulent intensities “critically” stretched flamelets are not a good model for leading points burning rates, at least for the low Reynolds number and Damköhler number of the direct numerical simulations utilized in this study. This work also suggests the need for continued development of model laminar geometries to understand different turbulent structures. In addition to the unsteady effects emphasized above, which have been incorporated into various stretched flame analyses [59], there is a need for model flamelet geometries with saddle-point features (where k_1 and k_2 may be strongly non-zero, but $k_1 + k_2 \sim 0$), as well as those with a negative curvature-strain correlation.

Acknowledgments

This research was supported by the University Turbine Systems Research (contract #DE-FC21-92MC29061) program and the Air Force Office of Scientific Research (contract #FA9550-12-1-0107/RC657), contract monitors are Dr. Mark Freeman and Dr. Chiping Li, respectively. The authors gratefully acknowledge the help of Prof. C.J. Sung in making available the modified OPPDIF code used to simulate the counterflow tubular flame geometry.

References

[1] A.J. Aspden, M.S. Day, J.B. Bell, Turbulence–flame interactions in lean premixed hydrogen: transition to the distributed burning regime, J. Fluid Mech. 1 (1) (2011) 1–34.
[2] A.N. Lipatnikov, J. Chomiak, Molecular transport effects on turbulent flame propagation and structure, Progress Energy Combust. Sci. 31 (1) (2005) 1–73.
[3] D. Bradley, M. Lawes, K. Liu, M.S. Mansour, Measurements and correlations of turbulent burning velocities over wide ranges of fuels and elevated pressures, Proc. Combust. Inst. 34 (1) (2013) 1519–1526.
[4] C.K. Law, C.J. Sung, Structure, aerodynamics, and geometry of premixed flamelets, Progress Energy Combust. Sci. 26 (4) (2000) 459–505.
[5] S. Candel, T. Poinsot, Flame stretch and the balance equation for the flame area, Combust. Sci. Technol. 70 (1-3) (1990) 1–15.
[6] P. Clavin, Dynamic behavior of premixed flame fronts in laminar and turbulent flows, Progress Energy Combust. Sci. 11 (1) (1985) 1–59.
[7] T. Poinsot, T. Echekki, M.G. Mungal, A study of the laminar flame tip and implications for premixed turbulent combustion, Combust. Sci. Technol. 81 (1-3) (1992) 45–73.
[8] T.C. Lieuwen, Unsteady Combustor Physics, Cambridge University Press, 2012.
[9] M. Baum, T. Poinsot, D.C. Haworth, N. Darabiha, Direct numerical simulation of $H_2/O_2/N_2$ flames with complex chemistry in two-dimensional turbulent flows, J. Fluid Mech. 281 (1994) 1–32.

[10] E.R. Hawkes, J.H. Chen, Direct numerical simulation of hydrogen-enriched lean premixed methane–air flames, Combust. Flame 138 (3) (2004) 242–258.
[11] E.R. Hawkes, J.H. Chen, Comparison of direct numerical simulation of lean premixed methane–air flames with strained laminar flame calculations, Combust. Flame 144 (1) (2006) 112–125.
[12] R. Sankaran, E.R. Hawkes, J.H. Chen, T. Lu, C.K. Law, Structure of a spatially developing turbulent lean methane–air Bunsen flame, Proc. Combust. Inst. 31 (1) (2007) 1291–1298 http://dx.doi.org/10.1016/j.proci.2006.08.025 .
[13] D. Bradley, P. Gaskell, A. Sedaghat, X. Gu, Generation of PDFS for flame curvature and for flame stretch rate in premixed turbulent combustion, Combust. Flame 135 (4) (2003) 503–523.
[14] T. Poinsot, S. Candel, A. Trouvé, Applications of direct numerical simulation to premixed turbulent combustion, Progress Energy Combust. Sci. 21 (6) (1995) 531–576.
[15] D.C. Haworth, T. Poinsot, Numerical simulations of Lewis number effects in turbulent premixed flames, J. Fluid Mech. 244 (1) (1992) 405–436.
[16] N. Chakraborty, R.S. Cant, Effects of strain rate and curvature on surface density function transport in turbulent premixed flames in the thin reaction zones regime, Phys. Fluids 17 (2005) 065108.
[17] N. Chakraborty, R.S. Cant, Unsteady effects of strain rate and curvature on turbulent premixed flames in an inflow–outflow configuration, Combust. Flame 137 (1–2) (2004) 129–147.
[18] N. Chakraborty, R.S. Cant, Influence of Lewis number on curvature effects in turbulent premixed flame propagation in the thin reaction zones regime, Phys. Fluids 17 (2005) 105105.
[19] N. Chakraborty, R.S. Cant, Influence of Lewis number on strain rate effects in turbulent premixed flame propagation, Int. J. Heat Mass Transf. 49 (13–14) (2006) 2158–2172.
[20] S.H. Kim, H. Pitsch, Scalar gradient and small-scale structure in turbulent premixed combustion, Phys. Fluids 19 (11) (2007) 115104.
[21] B. Renou, A. Boukhalfa, D. Puechberty, M. Trinité, Effects of stretch on the local structure of preely propagating premixed low-turbulent flames with various lewis numbers, Symp. (Int.) Combust. 27 (1) (1998) 841–847 http://dx.doi.org/10.1016/S0082-0784(98)80480-3.
[22] A. Trouvé, T. Poinsot, The evolution equation for the flame surface density in turbulent premixed combustion, J. Fluid Mech. 278 (-1) (1994) 1–31.
[23] N. Chakraborty, R.S. Cant, Effects of Lewis number on flame surface density transport in turbulent premixed combustion, Combust. Flame 158 (2011) 1768–1787.
[24] G. Damköhler, The effect of turbulence on the flame velocity in gas mixtures, Zeitschrift Electrochem 46 (1940) 601–626.
[25] R.W. Bilger, S.B. Pope, K.N.C. Bray, J.F. Driscoll, Paradigms in turbulent combustion research, Proc. Combust. Inst. 30 (1) (2005) 21–42.
[26] I. Zeldovich, G.I. Barenblatt, V. Librovich, G. Makhviladze, Mathematical Theory of Combustion and Explosions, Consultants Bureau, Plenum Publishing Corporation, New York, 1985.
[27] V.P Karpov, A.N. Lipatnikov, V.L. Zimont, Flame curvature as a determinant of preferential diffusion effects in premixed turbulent combustion, in: B. Zel'dovich, W.A. Sirignano, A.G. Merzhanov, L. De Luca (Eds.), Advances in Combustion Science: in Honor of YA, AIAA, 1997.
[28] N.K. Aluri, S.P.R. Muppala, F. Dinkelacker, Substantiating a fractal-based algebraic reaction closure of premixed turbulent combustion for high pressure and the Lewis number effects, Combust. Flame 145 (4) (2006) 663–674.
[29] V. Karpov, A. Lipatnikov, V. Zimont, The Combustion Institute, Pittsburg, PA (1996) 249
[30] F. Dinkelacker, B. Manickam, S.P.R. Muppala, Modelling and simulation of lean premixed turbulent methane/hydrogen/air flames with an effective Lewis number approach, Combust. Flame 158 (9) (2011) 1742–1749.
[31] N.K. Aluri, S.P.R. Muppala, F. Dinkelacker, Large-eddy simulation of lean premixed turbulent flames of three different combustion configurations using a novel reaction closure, Flow, Turbul. Combust. 80 (2) (2008) 207–224.
[32] V.P. Karpov, A.N. Lipatnikov, V.L. Zimont, A test of an engineering model of premixed turbulent combustion, Symp. (Int.) Combust. 26 (1) (1996) 249–257.
[33] A.N. Lipatnikov, J. Chomiak, Lewis number effects in premixed turbulent combustion and highly perturbed laminar flames, Combust. Sci. Technol. 137 (1-6) (1998) 277–298.
[34] V.R. Kuznetsov, V.A. Sabel'nikov, Turbulence and Combustion, Hemisphere Publishing, New York, 1990.
[35] P. Venkateswaran, A. Marshall, D.H. Shin, D. Noble, J. Seitzman, T. Lieuwen, Measurements and analysis of turbulent consumption speeds of H_2/CO mixtures, Combust. Flame 158 (8) (2011) 1602–1614.
[36] P. Venkateswaran, A. Marshall, J. Seitzman, T. Lieuwen, Pressure and fuel effects on turbulent consumption speeds of H_2/CO blends, Proc. Combust. Inst. 34 (2013) 1527–1535.
[37] P. Venkateswaran, A. Marshall, J. Seitzman, T. Lieuwen, Turbulent consumption speeds of high hydrogen content fuels from 1-20 atm, J. Eng. Gas Turbines Power 136 (2014) 011504.
[38] S.P.R. Muppala, M. Nakahara, N.K. Aluri, H. Kido, J.X. Wen, M.V. Papalexandris, Experimental and analytical investigation of the turbulent burning velocity of two-component fuel mixtures of hydrogen, methane and propane, Int. J. Hydrogen Energy 34 (22) (2009) 9258–9265.
[39] F.T. Yuen, Ö.L. Gülder, Turbulent premixed flame front dynamics and implications for limits of flamelet hypothesis, Proc. Combust. Inst. 34 (2012) 1393–1400.
[40] A. Amato, M.S. Day, J.B. Bell, R.K. Cheng, T. Lieuwen, Leading Edge Statistics of Turbulent, Lean, H_2/Air Flames, Proc. Combust. Inst. (2014).
[41] D.M. Mosbacher, J.A. Wehrmeyer, R.W. Pitz, C.J. Sung, J.L. Byrd, Experimental and numerical investigation of premixed tubular flames, Proc. Combust. Inst. 29 (2) (2002) 1479–1486.
[42] C.T. Bowman, R.K. Hanson, D.F. Davidson, W.C.J. Gardiner, V. Lissianski, G.P. Smith, D.M. Golden, M. Frenklach, M. Goldenberg GRI-Mech 2.11. http://www.me.berkeley.edu/gri_mech/
[43] R.J. Kee, J. Warnatz, J.A. Miller, Fortran computer-code package for the evaluation of gas-phase viscosities, conductivities, and diffusion coefficients, Sandia report SAND83-8209 (1983)
[44] A. Amato, Leading Points Concepts in Turbulent Premixed Combustion Modeling. PhD thesis, Georgia Institute of Technology, 2014.
[45] R.J. Kee, J.F. Grcar, M.D. Smooke, J.A. Miller, PREMIX: a Fortran program for modeling steady laminar one-dimensional premixed flames, Sandia Report, 1985 SAND85-8240.
[46] M.S. Day, J.B. Bell, P.T. Bremer, V. Pascucci, V. Beckner, M. Lijewski, Turbulence effects on cellular burning structures in lean premixed hydrogen flames, Combust. Flame 156 (5) (2009) 1035–1045.
[47] R.J. Kee, F.M. Rupley, E. Meeks, J.A. Miller, CHEMKIN III: A FORTRAN Chemical Kinetics Package for the analysis of Gas-Phase Chemical and Plasma Kinetics, Sandia report, SAND96-8216 (1996).
[48] D. Bradley, P. Gaskell, X. Gu, Burning velocities, Markstein lengths, and flame quenching for spherical methane-air flames: a computational study, Combust. Flame 104 (1) (1996) 176–198.
[49] Z. Chen, M.P. Burke, Y. Ju, Effects of Lewis number and ignition energy on the determination of laminar flame speed using propagating spherical flames, Proc. Combust. Inst. 32 (1) (2009) 1253–1260.
[50] Z. Chen, Y. Ju, Theoretical analysis of the evolution from ignition kernel to flame ball and planar flame, Combust. Theory Model. 11 (3) (2007) 427–453.
[51] Y.C. Chen, R.W. Bilger, Experimental investigation of three-dimensional flame-front structure in premixed turbulent combustion: II. Lean hydrogen/air Bunsen flames, Combust. Flame 138 (1–2) (2004) 155–174 http://dx.doi.org/10.1016/j.combustflame.2004.04.009.
[52] C. Rutland, A. Trouvé, Direct simulations of premixed turbulent flames with nonunity Lewis numbers, Combust. Flame 94 (1-2) (1993) 41–57.
[53] M. Katragadda, S.P. Malkeson, N. Chakraborty, Modelling of the tangential strain rate term of the Flame Surface Density transport equation in the context of Reynolds Averaged Navier–Stokes simulation, Proc. Combust. Inst. 33 (1) (2011) 1429–1437 http://dx.doi.org/10.1016/j.proci.2010.06.129 .
[54] C. Meneveau, T. Poinsot, Stretching and quenching of flamelets in premixed turbulent combustion, Combust. Flame 86 (4) (1991) 311–332 http://dx.doi.org/10.1016/0010-2180(91)90126-V .
[55] S.B. Pope, The evolution of surfaces in turbulence, Int. J. Eng. Sci. 26 (5) (1988) 445–469.
[56] R.S. Cant, Direct numerical simulation of premixed turbulent flames, Phys. Eng. Sci. 357 (1764) (1999) 3583–3604.
[57] M. Tanahashi, M. Fujimura, T. Miyauchi, Coherent fine-scale eddies in turbulent premixed flames, Proc. Combust. Inst. 28 (1) (2000) 529–535.
[58] J.H. Chen, H.G. Im, Stretch effects on the burning velocity of turbulent premixed hydrogen/air flames, Proc. Combust. Inst. 28 (1) (2000) 211–218.
[59] H.G. Im, J.H. Chen, Effects of flow transients on the burning velocity of laminar hydrogen/air premixed flames, Proc. Combust. Inst. 28 (2) (2000) 1833–1840.
[60] B. Savard, G. Blanquart, An a priori model for the effective species Lewis numbers in premixed turbulent flames, Combustion and Flame (2014) http://dx.doi.org/10.1016/j.combustflame.2013.12.014.